Article

http://justc.ustc.edu.cn

# Flow-induced vibration of plate and cylinder under unilateral spring constraint

Zhe Chen, and An-Kang Gao ✉

*Department of Modern Mechanics, University of Science and Technology of China, Hefei 230027, Anhui, China*

✉Correspondence: An-Kang Gao, E-mail: ankanggao@ustc.edu.cn


## Graphical abstract

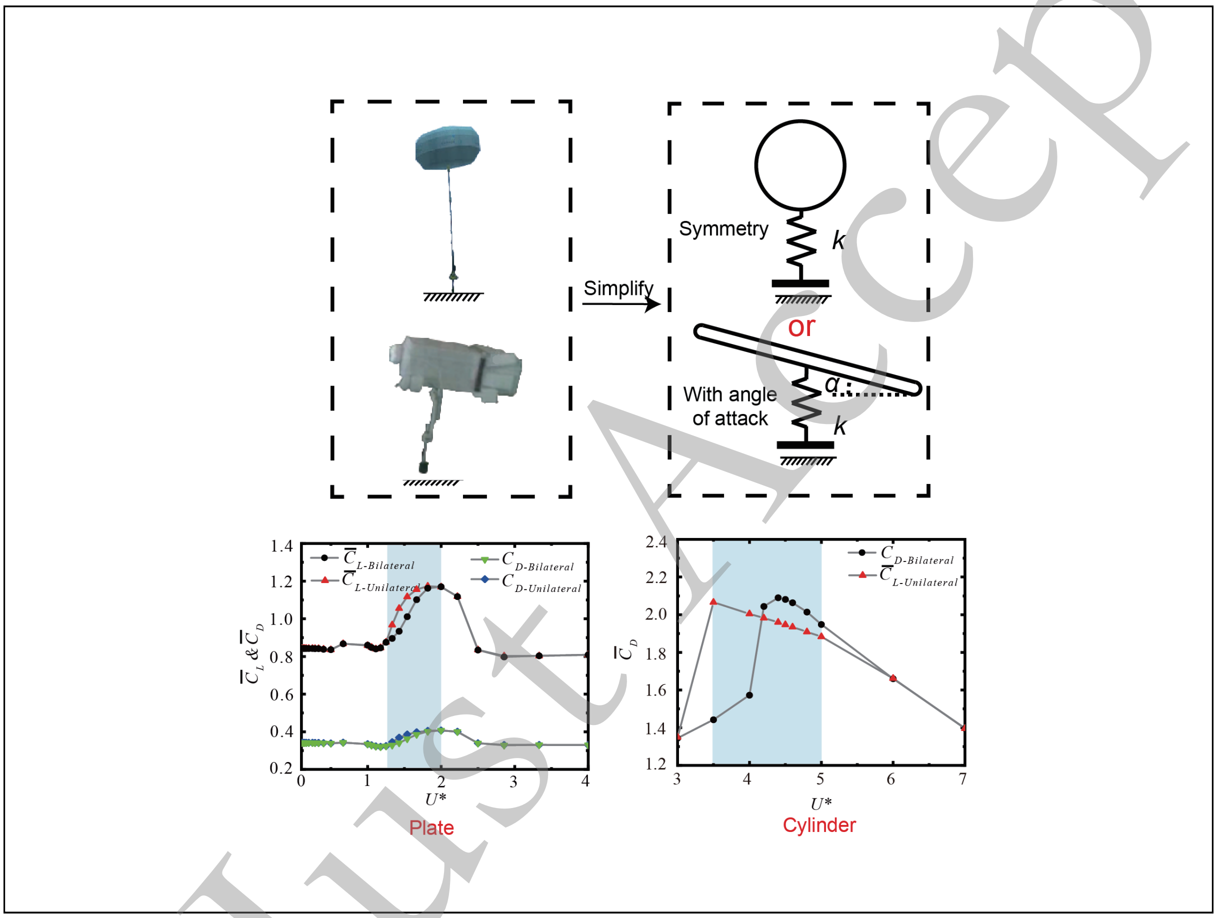


*Schematic diagram of unilateral constraint models and their hydrodynamic characteristics differences with bilateral constraints.*

## Public summary

- Exploring the jumping motion of underwater-legged robots using a simplified unilateral constraint model.
- There are significant differences in hydrodynamic characteristics under two types of constraints.
- The modified force element theory is used to explore the flow mechanisms that result in differences in hydrodynamic characteristics with bilateral and unilateral constraints.

**Citation:** Chen Z, Gao A K. Flow-induced vibration of plate and cylinder under unilateral spring constraint. *JUSTC*, **2026**, 55(0): . CSTR: 32290.14.JUSTC-2025-0023. DOI: 10.52396/JUSTC-2025-0023

JUSTC Article
http://justc.ustc.edu.cn

# Flow-induced vibration of plate and cylinder under unilateral spring constraint

Zhe Chen, and An-Kang Gao ✉

*Department of Modern Mechanics, University of Science and Technology of China, Hefei 230027, Anhui, China*

✉Correspondence: An-Kang Gao, E-mail: ankanggao@ustc.edu.cn


Cite This: *JUSTC*, **2026**, 55(X): (11pp)     Read Online     Supporting Information

**Abstract:** Flow-induced vibration (FIV) of an elastically mounted plate or cylinder under unilateral constraint is investigated using two-dimensional numerical simulations to explore the hydrodynamic force experienced by a body with spring-loaded legs resting on the seabed. For the unilateral constraint, the spring exerts force on the body only when it is compressed. Compared with bilateral constraint cases, distinct force features are observed. The plate exhibits an increased average lift, which is attributed to the increased vortex lift in the spring-compression phase. For the circular cylinder, an earlier transition from the initial branch to the lower branch is observed. The drag experienced by the cylinder is first increased for $U^* < 4.2$ and then reduced for $4.2 < U^* \leqslant 5$. By applying the modified force element theory, the mechanism for the different hydrodynamic behaviors under unilateral constraints has been identified, i.e., the changes in the vortex-shedding patterns and the vortex force. The findings may provide insights into the control strategies of underwater-legged robots, potentially leading to enhancements in their design and operational efficiency.

**Keywords:** Fluid-structure interaction; flow-induced vibration; unilateral constraint

**CLC number:**     **Document code:** A

## 1 Introduction

Underwater quadruped robots capable of walking, running, and jumping on the sea floor exhibit significant advantages in adapting to complex terrains and resisting water currents, positioning them as a hot point of research endeavors. Given that the density of the seawater is approximately 800 times that of the air, the resistance posed by water is not negligible. To analyze the dynamics of the underwater legged robot, Calisti et al.[1] proposed an underwater spring-loaded inverted pendulum (USLIP) model, and validated its rationale in single-legged[2] and quadruped underwater jumping robots[3]. In the USLIP model, the hydrodynamic force is simplified as the sum of the added mass force and a friction force whose dimensionless coefficient is a constant. In real situations, however, the unsteady vortex force generated by the vortex shedding has a significant effect on the body's motion[4] and inevitably results in a varying force coefficient. To address the influence of the vortex force, we study the flow-induced vibration (FIV) of two simplified models for underwater robots, a circular cylinder that mimics a symmetric bluff body and a flat plate that represents a slender body or a hydrofoil, with emphasis on the quantification and modeling of vortex force. The elastic leg is replaced with an infinitely thin and massless spring that only resists contraction, i.e. a unilateral spring constraint.

Although the FIV with a unilateral spring constraint is rarely explored, the FIV with a bilateral spring constraint, i.e. the spring exerts force on the body in both extension and contraction phases, has been extensively studied due to its importance in engineering applications[4–6]. Prasanth and Mittal[5] numerically simulated the FIV of a circular cylinder with a reduced mass of $2.5\pi$ ($M^* = M/(\rho D^2)$) in the laminar flow regime. They discovered that the shift in the phase between the lift history and the transverse displacement is dominantly affected by the pressure force. The viscous force, on the other hand, has the same phase as the displacement for all Reynolds numbers. Dorogi and Baranyi[7] studied the vortex-induced vibration of the cylinder with a mass ratio of $M^* = 10$ at $Re = 300$. They discovered that three branches exist in the cylinder's response: the initial branch, the lower branch, and the upper branch. To investigate the hydrodynamic characteristics of cylinders, Soti *et al.*[8] experimentally investigated the damping effects on the vortex-induced vibration (VIV) of a cylinder with a reduced mass of $M^* = 3$. They found a typical three-branch VIV response at low damping. After the fluid force is decomposed into potential force and the vortex-induced force, the two components show different trends with the change of reduced velocity in different branches. When the damping is low, the phase differences between the lift history and the displacement in the initial and upper branches are $0^\circ$ and $180^\circ$, respectively.

In general, bluff bodies are unfavorable for high lift and therefore are not suitable as control surfaces for underwater vehicles. In contrast, slender bodies such as airfoils manifest disparate FIV characteristics, which can be primarily ascribed to their high lift or thrust. Andersen *et al.*[9] studied the wake structure and thrust variation of airfoils in pure heaving motion and pure pitching motion. Results showed that the critical Strouhal number for thrust generation is $St = 0.28$ for the pitching motion, significantly higher than the critical Strouhal number for the emergence of reverse Bénard–von Kármán (BvK) vortex street; The thrust transition in the pure heaving motion coincides with the vortex street transition, which occurs at $St = 0.16$. From this, it can be seen that the pure heaving motion is more advantageous in thrust generation than the pure pitching motion. In addition, the FIV of a slender body can also be used in energy harvesting. Wu *et al*.[10] numerically investigated the semi-active flapping foil that performs an prescribed pitching motion with two auxiliary smaller foils. This work indicated that the increased lift force, resulting from the vortex-body interaction, leads to an enhanced power extraction, which directly contributes to efficiency improvement. Besem *et al*.[11] utilized a harmonic balance method to forecast the natural shedding frequency and lock-in region of an airfoil at high angles of attack (AoAs). Subsequently, their numerical findings are compared with experimental data obtained from wind tunnel tests, revealing a similar lock-in region. Gao *et al*.[12] conducted a numerical study on the lift force of an elastically mounted airfoil undergoing FIV in the vertical direction. Their investigation was conducted at a Reynolds number of 800 and involved high AoAs. The results revealed that a significant lift enhancement, amounting to as much as 35%, could be achieved when the reduced velocity approached a value of 2.

Inspired by underwater biomimetic quadruped robots, in this study, we focus on the behavior of a plate or a cylinder under unilateral spring constraint and submerged in a steady uniform flow. The vertical motion of the body is determined by the interaction between the fluid and the structure, whereas all other degrees of freedom (DoFs) are fixed. Our primary aim is to investigate the hydrodynamic characteristics of the plate and the cylinder. In particular, we concentrate on the FIV at low Reynolds numbers and across a wide range of reduced velocities.

The structure of the paper is as follows. Section 2 gives the problem definition and numerical method. Section 3 presents the time-dependent force, oscillatory motion, and vortex wake patterns of typical cases, followed by a comprehensive summary of their statistical features. In section 3.3, a force decomposition is conducted utilizing a modified force element theory to uncover the hydrodynamic force mechanisms. The key findings are briefly summarized in section 4.

## 2 Physical model and numerical method

A schematic illustration of the simplified model for an underwater-legged robot is provided in Fig. 1. The underwater biomimetic monopod robot displayed in the bottom left corner is reproduced from the work of Calisti et al.[1]. In this model, a cylinder or plate is chosen as the representative geometries for bluff or slender bodies, respectively. The legs of underwater robots are simplified as a unilateral constraint spring. Additionally, we assume that the legs of the objects are long enough to ignore the hydrodynamic interaction between the robot body and the bottom wall. Consequently, the model becomes an elastically mounted flat plate or cylinder submerged in a two-dimensional uniform flow $U_\infty$. This flow is

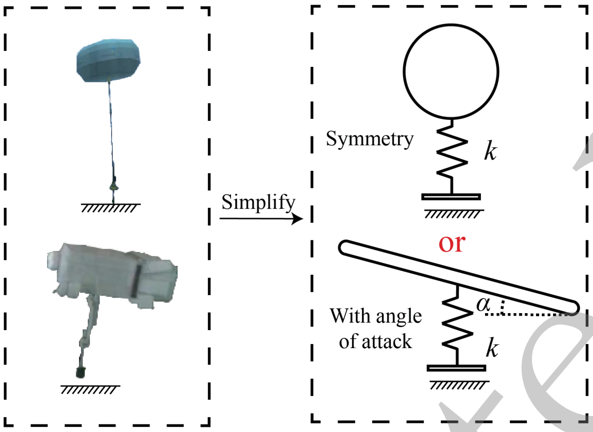


**Fig. 1.** Schematic show of an elastically mounted plate and cylinder simplified from underwater biomimetic quadruped robots and wave energy conversion devices.

characterized by its incompressible nature and constant density, $\rho$. We assume the body experiences FIV solely in the vertical direction, with its horizontal and rotational movements both fixed.

It is worth noting that the plate's thickness is set as 1/20 of the chord length $c$, a design choice that has been shown to enhance hydrodynamic performance at low Reynolds numbers, according to Sun et al.[13]. The flat plate has rounded leading and trailing edges.

The vertical motion of the body is determined by Newton's law of motion,

$$\begin{cases} M\ddot{y}_B + ky_B = F_y - (\rho_s - \rho)gV_B, & y_B \leqslant 0 \\ M\ddot{y}_B = F_y - (\rho_s - \rho)gV_B & y_B > 0 \end{cases} \tag{1}$$

where $M$ is the mass of the plate and cylinder, $k$ is the stiffness of the spring, $y_B = y_B(t)$ is the instantaneous vertical displacement, and $F_y$ is the lift force exerted by the fluid. Additionally, $V_B$ is the volume of the body and $g$ is the gravity acceleration, which is taken as $9.8\ \mathrm{m/s^2}$. $\rho_s$ and $\rho$ represent the density of the solid body and the fluid, respectively. Due to the unilateral constraint of the spring, its stiffness is set as zero when $y_B > 0$, indicating that the object leaves the sea floor and enters the free motion phase. It is important to note that we have implicitly assumed the absence of damping in the spring-mass system.

To avoid the requirement for a moving grid, the absolute flow velocity $\boldsymbol{u}$ is computed within the body frame of reference that is fixed on the body. Consequently, the governing equations for $\boldsymbol{u}$ are derived as[14]

$$\partial_t \boldsymbol{u} + (\boldsymbol{u} - \dot{y}_B \boldsymbol{e}_y)\cdot\nabla\boldsymbol{u} = -\frac{1}{\rho}\nabla p + \nu\nabla^2\boldsymbol{u}, \tag{2}$$

$$\nabla\cdot\boldsymbol{u} = 0. \tag{3}$$

Here, $\boldsymbol{e}_y$ is the unit base vector in the vertical direction and $\nu$ is the kinetic viscosity of the fluid with $\mu = \rho\nu$. On the body surface, the nonslip boundary condition applies, $\boldsymbol{u} = \dot{y}_B\boldsymbol{e}_y$. At the far field, the velocity recovers the uniform incoming flow, $\boldsymbol{u} = U_\infty\boldsymbol{e}_x$, where $\boldsymbol{e}_x$ is the unit base vector in the incoming flow direction.


CSTR: 32290.14.JUSTC-2025-0023
DOI: 10.52396/JUSTC-2025-0023
*JUSTC*, **2026**, 55(X):

Dimensionless parameters can be established by utilizing the incoming flow velocity $U_\infty$, the body length $c$, and the fluid density $\rho$ as the reference velocity, length, and density, respectively. The independent dimensionless parameters in this problem are the Reynolds number $Re$, the dimensionless mass $M^*$, the reduced velocity $U^*$, and the Froud number $Fr$. In particular, among these dimensionless numbers, "$c$" denotes the diameter of the cylinder or the chord length for the flat plate.

$$Re = \frac{U_\infty c}{\nu}, \quad M^* = \frac{M}{\rho c^2}, \quad U^* = \frac{U_\infty}{f_n c}, \quad Fr = \frac{U_\infty}{\sqrt{gc}} \tag{4}$$

where

$$f_n = \frac{1}{2\pi}\sqrt{\frac{k}{M}} \tag{5}$$

is the natural frequency of the mass-spring system in the vacuum. It should be noted that equation (5) is the natural frequency of the bilateral constraint system in the vacuum. The natural frequency of the unilateral system, as shown in Appendix D, is different from equation (5) and it depends on the maximum jumping height of the body. To compare the behaviors of the unilateral and bilateral systems more conveniently, we adopt a uniform reference frequency of $f_n$ for all cases.

In this work, the Reynolds number of the flat plate is fixed at 800, the AoA is 15° and the dimensionless mass is 1. The reduced velocity has a range $0 < U^* \leqslant 10$. For the cylinder, the Reynolds number is fixed at 150, and the dimensionless mass is 2. The reduced velocity is $3 < U^* \leqslant 8$. The Froud number is fixed at 1. The rigidity of the spring decreases with the reduced velocity. For $U^* = 0$, the body is fixed and for $U^* = \infty$, the body is set as free. In the following discussions, the dimensionless quantities are marked using a superscript "*" unless otherwise specified.

## 3 Results

### 3.1 Time-dependent flow

To understand the effect of FIV on the hydrodynamic performance, the transient lift and drag coefficients of both the flat plate and the cylinder are first investigated. The specific parameters are $U^* = 1.54$, $Re = 800$, $M^* = 1$ for the plate, and $U^* = 4$, $Re = 150$, $M^* = 2$ for the cylinder. For comparison, the bilateral case is also simulated and its temporal phase has been shifted so that the first maximum displacement coincides with the unilateral constraint case. As shown in Fig. 2, where blue-shaded areas indicate the free motion phases, the appearance of the free motion phase reduces the oscillation frequency, and the overall displacement of the body has been shifted upwards. Due to the discontinuity in the time derivative of the body acceleration, there is a notable change in the slope of the lift coefficient after the body leaves the sea floor.

For the plate, as shown in Fig. 2a and Fig. 2b, although the

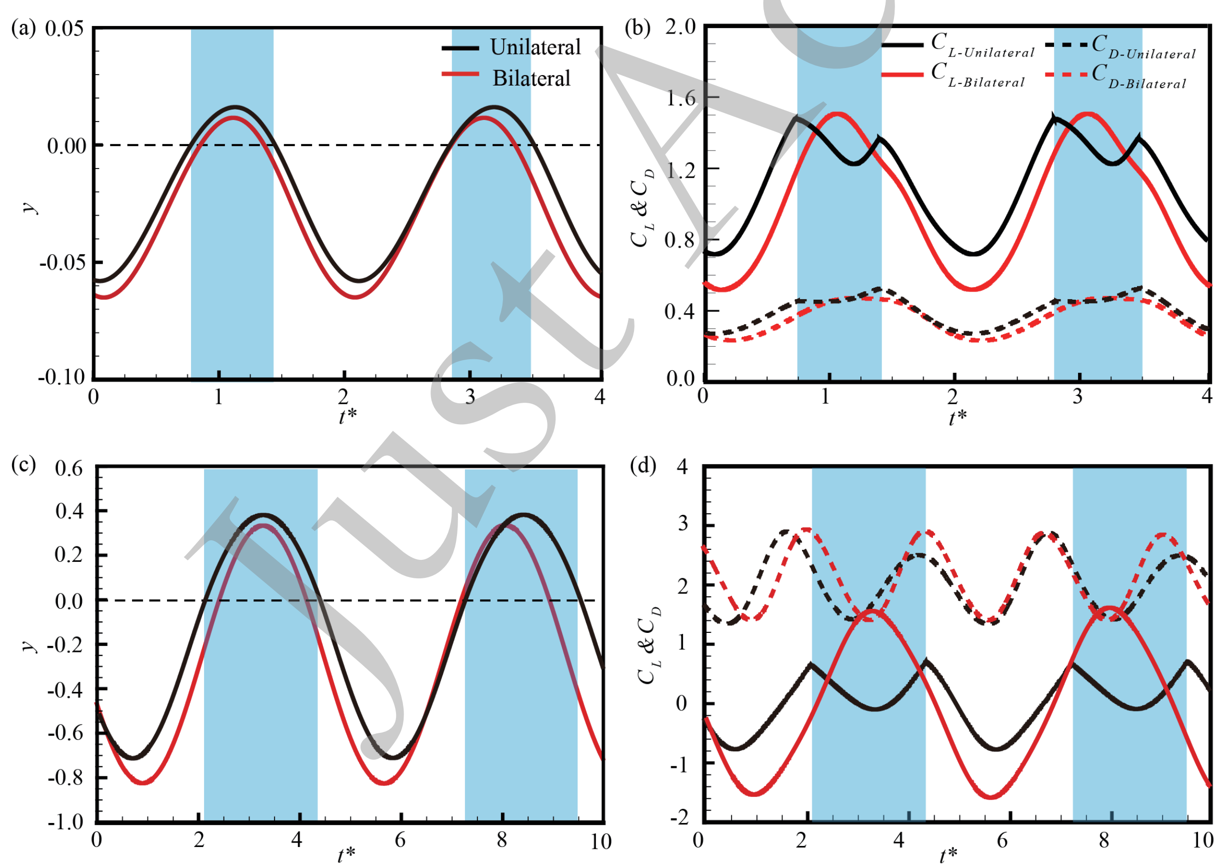


**Fig. 2.** Time-dependent vertical displacement and force coefficients. (a, b) Plate. (c, d) Circular cylinder. The blue-shaded areas indicate the body leaves the sea floor in the unilateral constraint cases.




CSTR: 32290.14.JUSTC-2025-0023
DOI: 10.52396/JUSTC-2025-0023
*JUSTC*, **2026**, 55(X):

free motion phase prevents the lift from further increasing, it also significantly reduces the lift drop in the spring-compression stage, resulting in an average lift higher than the bilateral case. The drag exhibits a similar trend as the lift, however, its variation magnitude is much smaller. Therefore, the lift-to-drag ratio is increased with the unilateral constraint.

The transient curves for the cylinder are depicted in Fig. 2c and Fig. 2d. Being similar to the plate, the free motion also prevents the lift of the cylinder from further increasing, and the subsequent spring compression stage prevents a decrease in lift. A temporary negative lift is experienced when the cylinder reaches the maximum displacement. Due to the symmetry of the cylinder, the frequency of the drag is twice that of the lift. Throughout the upward-moving stage, there is negligible variation in the drag coefficient when compared with the bilateral case, whereas a significant drag reduction is observed during the downward-moving stage, resulting in a decrease in the second drag peak.

Subsequently, Fig 3 depicts the vorticity fields of the plate and the cylinder at the maximum displacement. The leading-edge vortex (LEV) and trailing-edge vortex (TEV) shed from the plate form a vortex pair, resulting in a wake pattern of one pair (1P). Owing to the stronger intensity of the LEV, the self-induced velocity of the LEV-TEV pair directs upwards, resulting in an upward deflected wake. Compared to bilateral constraints, the decrease in plate acceleration leads to an increase in its period, ultimately causing the LEV to move a longer distance on the plate surface during the upward-moving stage. For the cylinder, two single vortices are shed in each period resulting in a classical Bénard–von Kármán (BvK) vortex street. Due to the longer period of the unilateral constraint case, the vortex generated in the downstroke stage moves further downstream when the cylinder reaches the maximum displacement. The reduced interaction between the previous vortex and the cylinder leads to a more dispersed vortex formation in the upstroke stage.

### 3.2 Time-averaged flow

To gain a deeper understanding on the effect of FIV, the time-averaged force coefficients and the peak-to-peak amplitude $A_y^*$ are analyzed. It should be noted that the stiffness of the spring that connects the body decreases with the increasing $U^*$. Specifically, $U^* = 0$ indicates the body is fixed.

The time-averaged force coefficients, the peak-to-peak amplitude and the dominant vibration frequency of the flat plate at $Re = 800$ and $M^* = 1$ are shown in Fig. 4a and Fig. 4b. For most unilateral constrained cases, the data are exactly the same as the bilateral constraint cases because the maximum vertical position of the plate does not exceed zero and, as a result, the body never leaves the sea floor. When the reduced velocity is in the range of $1.33 < U^* \leqslant 2$, the time-averaged lift and drag coefficients become larger than bilateral constraint cases. The vibration period also becomes slightly larger as indicated by the frequency plot. Specifically, when the reduced velocity is around 1.4, a lift enhancement of up to 13% is achieved compared with the bilateral constraint case. The difference in the vibration amplitude is relatively small between the two constraints. With the increasing reduced velocity, the peak-to-peak amplitude of the unilateral case is first slightly smaller than that of the bilateral case and then becomes slightly larger after $U^* > 1.54$.

The time-averaged force coefficients, the peak-to-peak amplitude and the dominating vibration frequency of the cylinder at $Re = 150$ and $M^* = 2$ are shown in Fig. 4c and Fig.

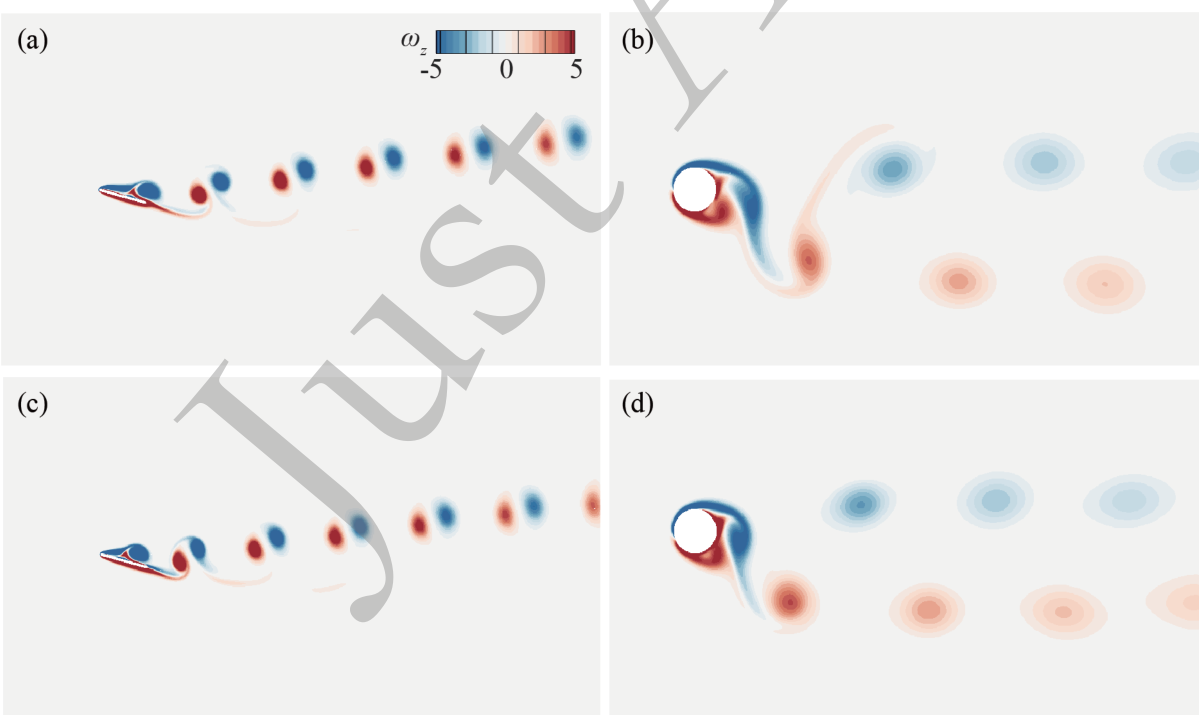


**Fig. 3.** Vorticity fields when the body is at the maximum displacement. (a) Plate, unilateral, (b) cylinder, unilateral, (c) plate, bilateral, (d) cylinder, bilateral.




CSTR: 32290.14.JUSTC-2025-0023
DOI: 10.52396/JUSTC-2025-0023
*JUSTC*, **2026**, 55(X):

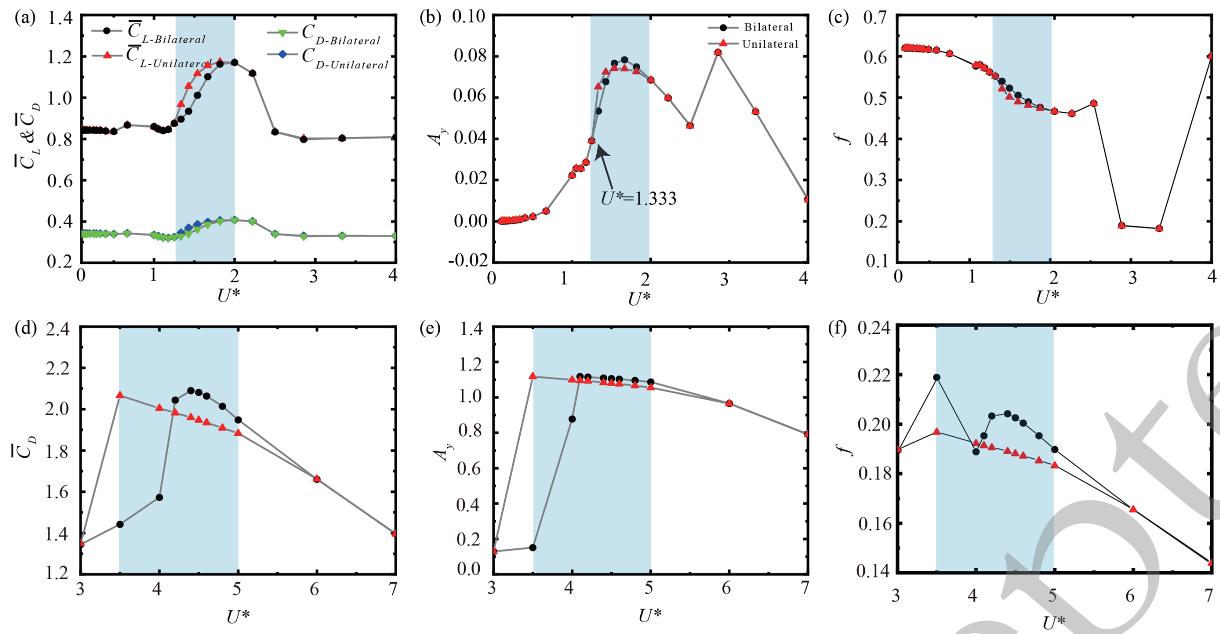


**Fig. 4.** Time-averaged force coefficients, the peak-to-peak vibration amplitude and dominant vibration frequency. (a, b, c) Flat plate. (d, e, f) circular cylinder. The blue-shaded areas indicate the body leaves the sea floor in the unilateral constraint cases.

4d. Due to the low Reynolds number, only the initial and lower branches are observed. It is apparent that within the reduced velocity range of 3.5 to 5, the drag coefficient of the cylinder exhibits a notable difference between the two constraints. The unilateral constraints facilitate an earlier transition from the initial branch to the lower branch. The vibration frequency of the cylinder is significantly decreased, except for $U^*=4$. As the reduced velocity further increases and the cylinder reaches the lower branch, the drag coefficient initially surpasses that observed in the bilateral constraint scenario but eventually drops below it for $4.2<U^*\leqslant 5$. Nevertheless, it is worth noting that the vibration amplitude remains comparable between the unilateral and bilateral constraint cases within this $U^*$ range.

### 3.3 Insights from force decomposition

To reveal the hydrodynamic mechanisms, a modified force-element theory[15], whose volume integrand and surface integrands are all Galilean-invariant[16], is applied. In the modified force element theory, the hydrodynamic force can be expressed as follows:

$$F_i=\int_{V_f}2\rho Q\phi_i\mathrm{d}V+\int_{\partial B}-\rho\phi_i\boldsymbol{a}\cdot\boldsymbol{n}\mathrm{d}S+\int_{\partial B}\mu\phi_i\boldsymbol{n}\cdot\nabla^2\boldsymbol{u}\mathrm{d}S+\int_{\partial B}\mu(\omega\times\boldsymbol{n})\cdot\boldsymbol{e}_i\mathrm{d}S, \tag{6}$$

where $V_f$ is the entire fluid domain, $\partial B$ is the body surface, $\boldsymbol{a}$ is the fluid acceleration on the body surface, $\omega=\nabla\times\boldsymbol{u}=\omega_z\boldsymbol{e}_z$ is the vorticity vector, and $Q$ is the second invariant of the velocity gradient tensor. Note that $Q>0$ is commonly used for vortex identification, known as the “Q-criterion”[17].

In Eq. (6), $\phi_i$ is a weight function defined by the equation:

$$\nabla^2\phi_i=0 \tag{7}$$

in the fluid domain $V_f$. On the body surface $\partial B$, whose solid-to-fluid-pointing unit normal vector is denoted as $\boldsymbol{n}$, the boundary condition is $\nabla\phi_i\cdot\boldsymbol{n}=-\boldsymbol{e}_i\cdot\boldsymbol{n}$. At the infinitely far field, $\phi_i$ decays to zero, $\phi_i=0$. The weight function $\phi_i$ measures the importance of $2\rho Q$, which equals $\nabla^2p$, with respect to the spatial location. Due to the fast decay of $\phi_i$ in the far field, the volume integral in Eq. (6) can generally be truncated at three chord lengths[18]. Equation (7), along with its corresponding boundary conditions, is solved using the spectral/*hp* element method, implemented in the open-source code Nektar++[19].

The four terms on the right-hand side of Eq. (6) are designated as $F_{i,Q}$, $F_{i,a}$, $F_{i,p,vis}$ and $F_{i,f}$ respectively:

$$F_{i,Q}=\int_{V_f}2\rho Q\phi_i\mathrm{d}V, \tag{8}$$

$$F_{i,a}=\int_{\partial B}-\rho\phi_i\boldsymbol{a}\cdot\boldsymbol{n}\mathrm{d}S, \tag{9}$$

$$F_{i,p,vis}=\int_{\partial B}\mu\phi_i\boldsymbol{n}\cdot\nabla^2\boldsymbol{u}\mathrm{d}S, \tag{10}$$

$$F_{i,f}=\int_{\partial B}\mu(\omega_z\boldsymbol{e}_z\times\boldsymbol{n})\cdot\boldsymbol{e}_i\mathrm{d}S. \tag{11}$$

In incompressible flows, the pressure satisfies a Poisson equation $\nabla^2p=2\rho Q$ in the fluid domain and boundary condition $\boldsymbol{n}\cdot\nabla p=-\rho\boldsymbol{n}\cdot\boldsymbol{a}+\mu\boldsymbol{n}\cdot\nabla^2\boldsymbol{u}$ on the solid surface. Therefore, $F_{i,Q}$ represents the force resulting from the source of the pressure Poisson equation, $F_{i,a}$ represents the force due to the body acceleration, $F_{i,p,vis}$ represents the viscous effect in the Neumann-type pressure boundary condition on the solid surface $\partial B$, and $F_f$ is the friction force due to viscosity. $F_{i,Q}$ is also named vortex-induced force or vortex force due to its close relation with vortical structures identified by the Q criterion. Further details regarding Eq. (6) can be found in the work of Gao et al.[15] and Luo et al.[20].

The force decomposition based on Eq. (6) is shown in Fig. 5. The parameters selected for the plate and cylinder are the same as those in Section 3.1. Here, subscript $i$ is used to rep-




CSTR: 32290.14.JUSTC-2025-0023
DOI: 10.52396/JUSTC-2025-0023
*JUSTC*, **2026**, 55(X):

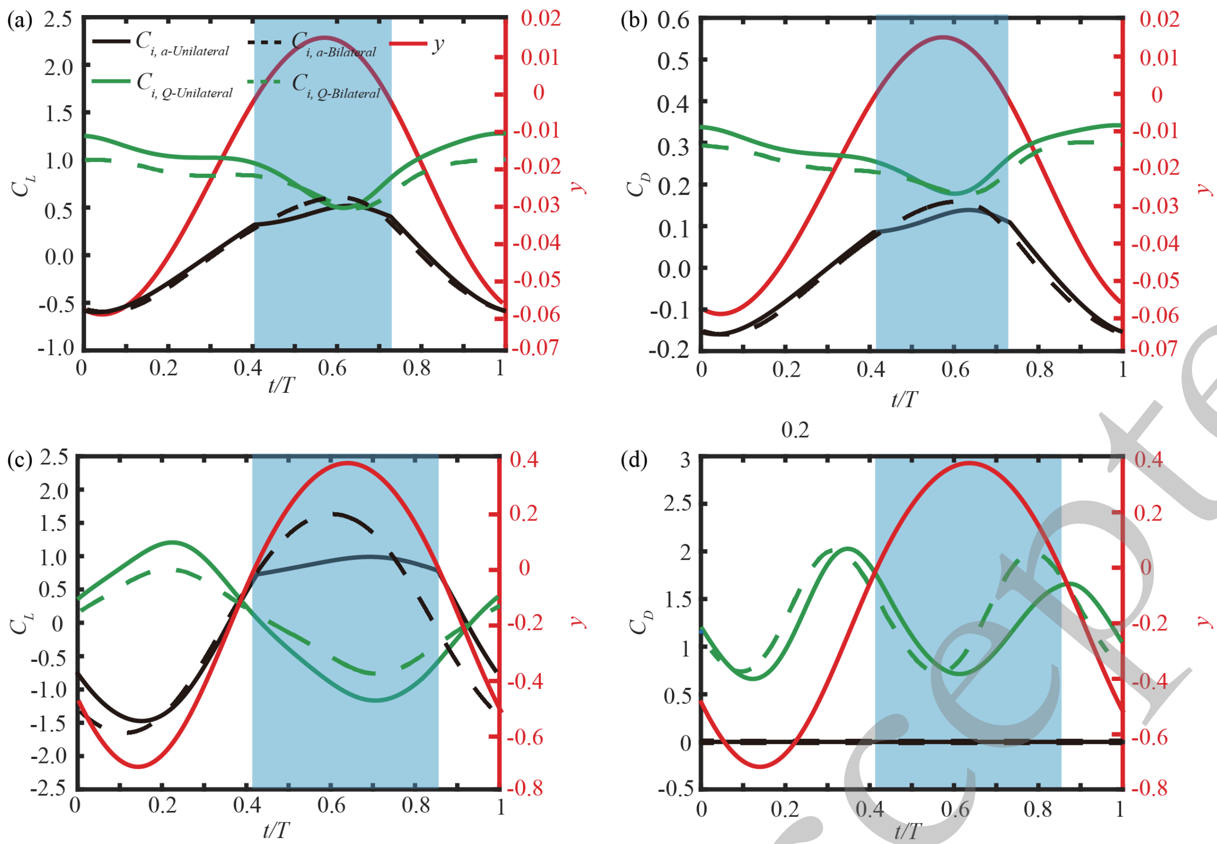


**Fig. 5.** Decomposition of time-dependent force coefficient. (a) plate lift coefficient, (b) plate drag coefficient, (c) cylinder lift coefficient, (d) cylinder drag coefficient. The blue-shaded areas indicate the body leaves the sea floor in the unilateral constraint cases.

resent the lift (L) or drag (D). The viscous-pressure force $C_{i,p,vis}$ and the friction force $C_{i,f}$ are very small and almost invariant at the current Reynolds number and therefore they are not presented in the figures. Consequently, it becomes evident that $C_{i,Q}$ and $C_{i,a}$ are the primary contributors to the force. In addition, as illustrated in Ref. [18], the $C_{i,a}$ has a zero mean value if the body only undergoes translational motion.

For the plate, $C_{i,Q}$ and $C_{i,a}$ are inversely related with a phase difference of $\pi$ for both lift and drag. The vortex force is maximized when the plate reaches the lowest displacement whereas the acceleration force is maximized when the plate is at the highest location. In the free motion phase, the $C_{L,a}$ and $C_{D,a}$ under unilateral constraint are both lower than them in the bilateral constraints case, whereas $C_{i,Q}$ remains almost unchanged. As a result, the lift and drag are reduced during the free motion phase, as indicated in Fig. 2a and Fig. 2b. During the spring-compression phase, the $C_{L,Q}$ under unilateral constraints is significantly higher, whereas there is only a smaller decrease in $C_{L,a}$, leading to an increase in the lift. Since the acceleration force has a zero mean value, the vortex force becomes the main source of the averaging force. It, therefore, can be concluded that the enhanced vortex force by the unilateral constraint during the spring compression phase is the main cause of the enhanced lift and lift-to-drag ratio.

For the cylinder, the $C_{L,Q}$ and $C_{L,a}$ are inversely related with a phase difference of about $\pi$. In the free motion phase where the maximum lift is achieved, both the acceleration lift and the vortex lift are reduced under the unilateral constraint, resulting in a reduced transient lift. In the spring compression phase where the lift force reaches the minimum value, the acceleration lift and the vortex lift are both increased under the unilateral constraints, as a result, an increased transient lift is observed. The overall effect results in a smaller fluctuation in the time-dependent lift coefficient for the unilateral constraint. Being different from the lift force, the vertical acceleration has no impact on the drag because of the geometric symmetry of the cylinder. Therefore, there is always $C_{D,a} = 0$, and the vortex force is the only dominating mechanism in drag production. The vortex drag shows the same phase in the two constraints. During the upward-moving phase, the value of the vortex drag shows no significant difference. However, during the following downward-moving half period, the vortex force increases significantly. This phenomenon agrees with the total drag shown in Fig. 2.

Additionally, we compute the integration of $2\rho Q\phi_i$ over a truncated fluid domain, $-3 \leqslant x/c \leqslant x_w, -3 \leqslant y/c \leqslant 3$. The corresponding force coefficient, denoted as $C_{L,Q}(x_w)$ and $C_{D,Q}(x_w)$, are depicted in Fig. 6. The analysis focuses on the instant when the maximum displacement is reached.

Our findings indicate that, for the plate, both $C_{L,Q}$ and $C_{D,Q}$ remain approximately zero for $x_w < -0.3c$. For $x_w > 2c$, the total force converges to the wall-stress integral result. As shown in Fig. 6a and Fig. 6b, in the front half of the plate, the lift and drag in the unilateral case are lower than those in the bilateral case. Conversely, in the rear half of the plate, the lift and drag in the unilateral case are higher than those in the bilateral case, which finally results in a similar total hydrodynamic force.




CSTR: 32290.14.JUSTC-2025-0023
DOI: 10.52396/JUSTC-2025-0023
*JUSTC*, **2026**, 55(X):

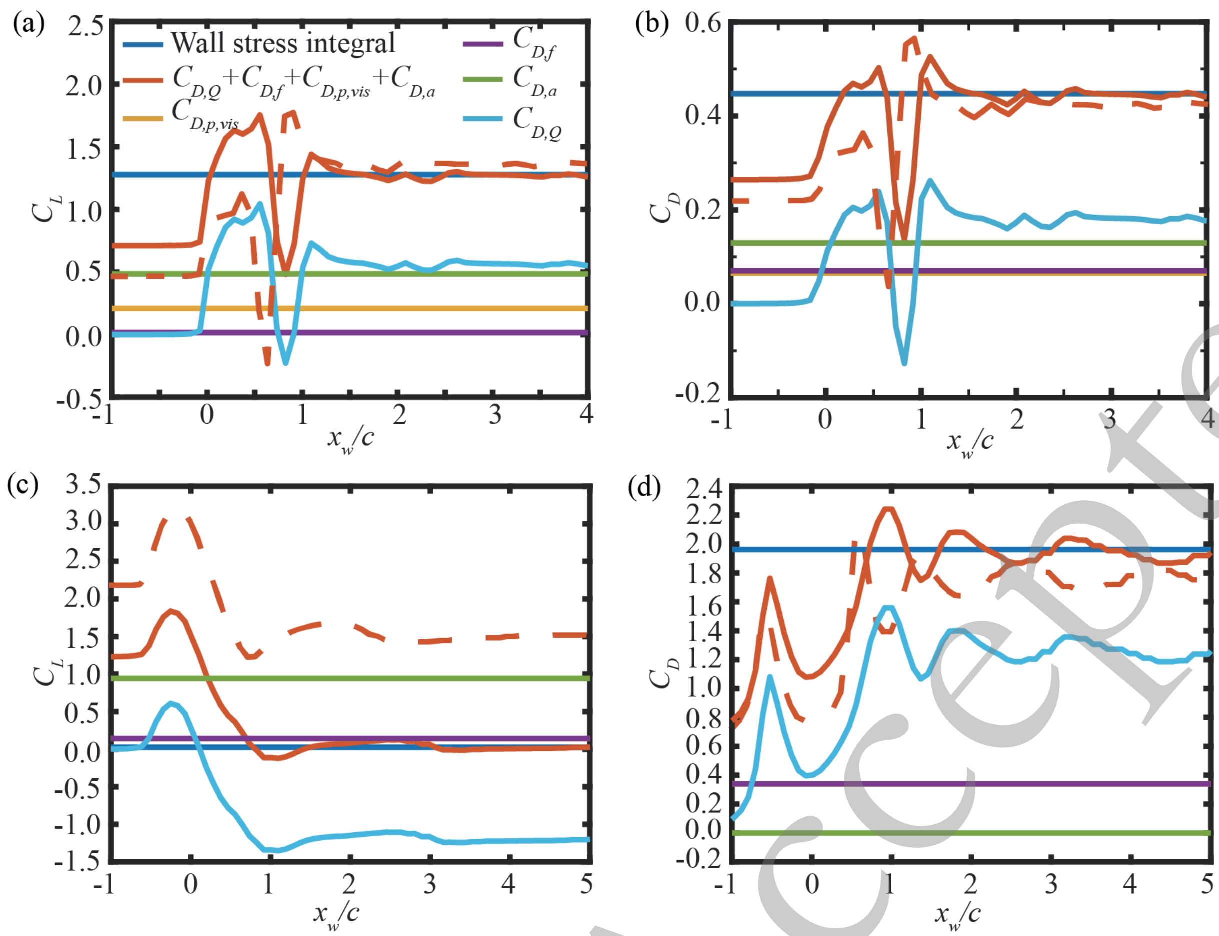


**Fig. 6.** Force decomposition at the maximum displacement moment for both plate and cylinder: (a) plate lift coefficient, (b) plate drag coefficient, (c) cylinder lift coefficient, (d) cylinder drag coefficient. The dashed line represents bilateral constraint cases.

For the cylinder, as shown in Fig. 6c and Fig. 6d, $C_{L,Q}$ remains nearly zero for $x_w < -0.5c$, and converges to the wall-stress integral for $x_w > 3c$. However, $C_{D,Q}$ requires a much larger domain to converge. A remarkable difference in lift exists between the unilateral and bilateral cases. This disparity is primarily attributed to the appearance of the free motion phase, which leads to a sharp decline in $C_{L,Q}$. Although unilateral constraint leads to a significant increase in drag near the surface of the cylinder, there is no significant difference in the final integration result.

Flow structures that contribute most to the hydrodynamic force are also examined from the contour plots of the volumetric force element $2\rho Q\phi_i$, normalized by $\rho U_\infty^2 c^{-1}$, see 7. Here, a positive volumetric force element indicates a positive contribution to the force from local flow structures and a negative value represents an opposite contribution.

For the plate depicted in Fig. 7a, as the fluid passes through the sharp leading edge, a strong strain-rate field on the lower surface generates a positive lift. Simultaneously, since $\phi_y$ exhibits opposite signs on the upper and lower surfaces, the shear layer with $Q > 0$ on the upper surface also contributes a positive lift. The combination of these effects, as illustrated by the integral curve in Figure 6a results in a prominent lift peak at the leading edge. However, despite the shear layer initiating a robust lift, this lift experiences a swift decrease owing to the presence of the LEV in the aft half of the plate. For the cylinder illustrated in Figure 7b, both $Q$ and $\phi_y$ exhibit the same sign at both the upstream and downstream regions, resulting in a significant increase in drag. Simultaneously, the wake produced by the cylinder has a substantial impact on the drag coefficient compared to that of the plate as shown in Fig. 6d.

## 4 Conclusions

In this study, two-dimensional numerical simulations are utilized to comprehensively investigate the hydrodynamic performance of elastically mounted plates and cylinders subject to unilateral constraints. The analysis is conducted at relatively low Reynolds numbers to explore the behavior of these structures in fluid-structure interaction scenarios.

Notably, when the plate enters the free motion phase, a remarkable lift enhancement occurs over a broader range of reduced velocity. Specifically, when the reduced velocity is around 1.4, a lift increase of up to 13% can be achieved compared with the bilateral constraint case. Imposing unilateral constraints significantly improved the overall lift.

Compared to the bilateral case, the presence of the free motion phase has advanced the emergence of the lower branch. Although this causes the drag of the cylinder to increase earlier, the drag is finally reduced when the reduced velocity is larger than 4.2.




CSTR: 32290.14.JUSTC-2025-0023
DOI: 10.52396/JUSTC-2025-0023
*JUSTC*, **2026**, 55(X):

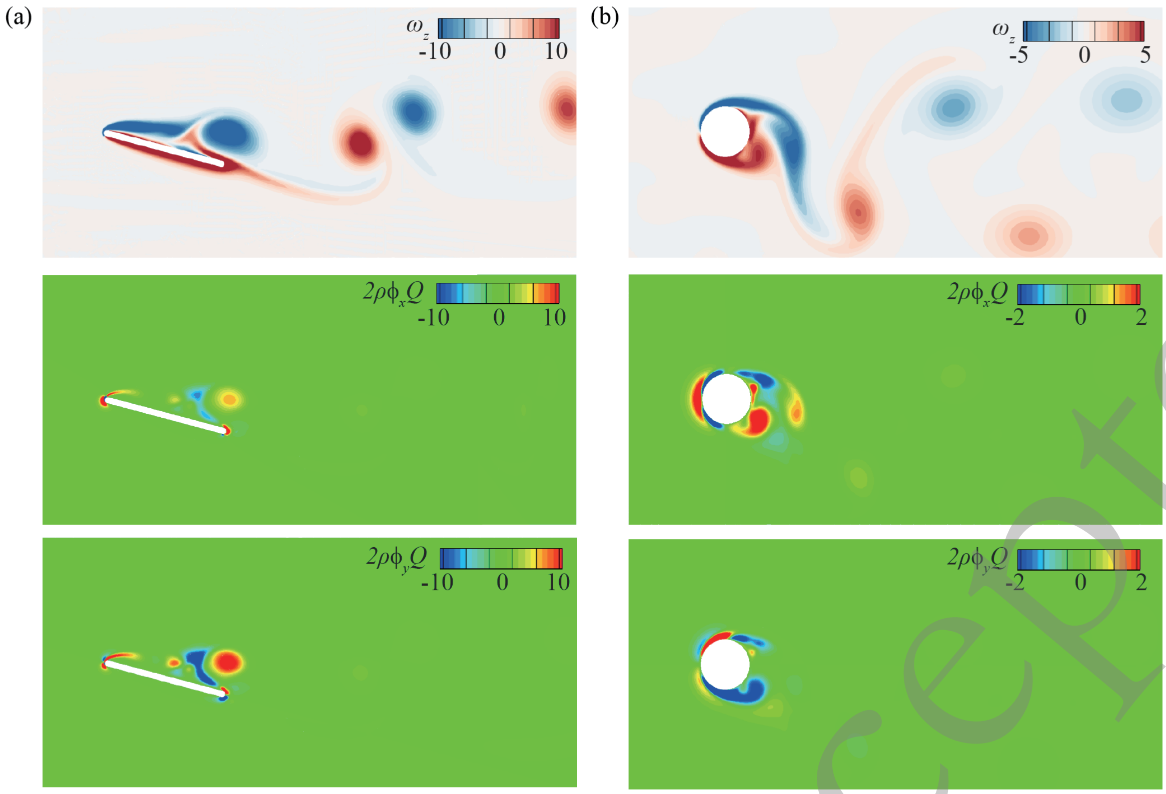


**Fig. 7.** Vorticity field and volumetric force elements. The upper panel shows the spanwise vorticity field. The middle panel shows the volumetric drag element and the Lower panel shows the volumetric lift element. (a) plate, (b) cylinder.

Through force decomposition analysis based on the modified force element theory, the cause of the performance improvement is explained. It's found that for the plate, $C_{i,Q}$ and $C_{i,a}$ have the main influence on its hydrodynamic force in the free motion phase and spring-compression phase, respectively. However, since the average value of acceleration force is usually 0, any changes in the average force should ultimately be caused by variations in vortex structure and vortex forces. For a cylinder, its lift is influenced by both $C_{i,Q}$ and $C_{i,a}$, but due to its geometric symmetry, its drag is only affected by $C_{i,Q}$.

Overall, this study highlights the importance of considering the unilateral constraint in the simplified model for underwater biomimetic quadruped robots. Future exploration could be made on the optimization of these systems, ultimately aiming to enhance their performance and adaptability in complex underwater environments.

## Conflict of Interest

The authors declare that they have no conflict of interest.

## Funding Information

This research was supported by the Fundamental Research Funds for the Central Universities (WK2090000054). We thank the USTC supercomputing center for providing computational resources for this project.

## Biographies

**Zhe Chen** currently a graduate student in the Department of Modern Mechanics, University of Science and Technology of China, under the supervision of Prof. Xi-Yun Lu. His research mainly focuses on fluid-structure interaction.

**An-Kang Gao** a Research Associate in the Department of Modern Mechanics, University of Science and Technology of China. His research mainly focuses on theoretical and computational fluid mechanics.

## References

[1] Calisti M, Falotico E, Laschi C. Hopping on uneven terrains with an underwater one-legged robot. *IEEE Robotics and Automation Letters*, **2016**, *1*: 461–468.

[2] Picardi G, Laschi C, Calisti M. Model-based open loop control of a multigait legged underwater robot. *Mechatronics*, **2018**, *55*: 162–170.

[3] Picardi G, Chellapurath M, Iacoponi S, et al. Bioinspired underwater legged robot for seabed exploration with low environmental disturbance. *Science Robotics*, **2020**, *5*: eaaz1012.

[4] Williamson C H K, Govardhan R. Vortex-induced vibrations. *Annual Review of Fluid Mechanics*, **2004**, *36*: 413–455.

[5] Prasanth T K, Mittal S. Vortex-induced vibrations of a circular cylinder at low Reynolds numbers. *Journal of Fluid Mechanics*, **2008**, *594*: 463–491.

[6] Ping H, Zhu H, Zhang K, et al. Vortex-induced vibrations of two rigidly coupled circular cylinders of unequal diameters at low Reynolds number. *Physics of Fluids*, **2021**, *33*: 103603.

[7] Dorogi D, Baranyi L. Identification of upper branch for vortex-induced vibration of a circular cylinder at Re = 300. *Journal of Fluids and Structures*, **2020**, *98*: 103135.

[8] Soti A K, Zhao J, Thompson M C, et al. Damping effects on vortex-induced vibration of a circular cylinder and implications for power extraction. *Journal of Fluids and Structures*, **2018**, *81*: 289–308.

[9] Andersen A, Bohr T, Schnipper T, et al. Wake structure and thrust





CSTR: 32290.14.JUSTC-2025-0023
DOI: 10.52396/JUSTC-2025-0023
*JUSTC*, **2026**, 55(X):

generation of a flapping foil in two-dimensional flow. *Journal of Fluid Mechanics*, **2017**, *812*: R4.
[10] Wu J, Chen Y L, Zhao N. Role of induced vortex interaction in a semi-active flapping foil based energy harvester. *Physics of Fluids*, **2015**, *27*: 093601.
[11] Besem F M, Kamrass J D, Thomas J P, et al. Vortex-induced vibration and frequency lock-In of an airfoil at high angles of attack. *Journal of Fluids Engineering*, **2016**, *138*: 011204.
[12] Gao A K, Chen Z, Liu L, et al. Lift enhancement for airfoil at high angle of attack using flow-induced vibrations. *Physics of Fluids*, **2024**, *36*: 123604.
[13] Sun Q, Boyd I D. Flat-plate aerodynamics at very low Reynolds number. *Journal of Fluid Mechanics*, **2004**, *502*: 199–206.
[14] Son O, Gao A-K, Gursul I, et al. Leading-edge vortex dynamics on plunging airfoils and wings. *Journal of Fluid Mechanics*, **2022**, *940*: A28.
[15] Gao A K, Zou S F, Shi Y, et al. Passing-over leading-edge vortex: The thrust booster in heaving airfoil. *AIP Advances*, **2019**, *9*: 035314.
[16] Gao A K, Wu J. A note on the Galilean invariance of aerodynamic force theories in unsteady incompressible flows. *Acta Mechanica Sinica*, **2019**, *35*: 1150–1154.
[17] Jeong J, Hussain F. On the identification of a vortex. *Journal of Fluid Mechanics*, **1995**, *285*: 69–94.
[18] Gao A K, Cantwell C D, Son O, et al. Three-dimensional transition and force characteristics of low-Reynolds-number flows past a plunging airfoil. *Journal of Fluid Mechanics*, **2023**, *973*: A43.
[19] Cantwell C D, Moxey D, Comerford A, et al. Nektar++: An open-source spectral/hp element framework. *Computer Physics Communications*, **2015**, *192*: 205–219.
[20] Luo X G, Gao A K, Lu X Y. Enhanced performance of a self-propelled flexible plate by a uniform shear flow and mechanism insight. *Physics of Fluids*, **2023**, *35*: 021903.
[21] Karniadakis G E, Israeli M, Orszag S A. High-order splitting methods for the incompressible Navier-Stokes equations. *Journal of Computational Physics*, **1991**, *97*: 414–443.
[22] Tufo H M, Fischer P F. Fast parallel direct solvers for coarse grid problems. *Journal of Parallel and Distributed Computing*, **2001**, *61*: 151–177.
[23] Orszag S A, Israeli M, Deville M O. Boundary conditions for incompressible flows. *Journal of Scientific Computing*, **1986**, *1*: 75–111.
[24] Moura R C, Aman M, Peiró J, et al. Spatial eigenanalysis of spectral/hp continuous Galerkin schemes and their stabilisation *via* DG-mimicking spectral vanishing viscosity for high Reynolds number flows. *Journal of Computational Physics*, **2020**, *406*: 109112.
[25] Newmark N M. A method of computation for structural dynamics. *Journal of the Engineering Mechanics Division*, **1959**, *85*: 67–94.
[26] Hou G, Wang J, Layton A. Numerical methods for fluid-structure interaction: A review. *Communications in Computational Physics*, **2012**, *12*: 337–377.
[27] Ahn H T, Kallinderis Y. Strongly coupled flow/structure interactions with a geometrically conservative ALE scheme on general hybrid meshes. *Journal of Computational Physics*, **2006**, *219*: 671–696.
[28] Borazjani I, Sotiropoulos F. Vortex-induced vibrations of two cylinders in tandem arrangement in the proximity–wake interference region. *Journal of Fluid Mechanics*, **2009**, *621*: 321–364.
[29] Bao Y, Zhou D, Tu J. Flow interference between a stationary cylinder and an elastically mounted cylinder arranged in proximity. *Journal of Fluids and Structures*, **2011**, *27*: 1425–1446.

# Appendix

## A Spectral/*hp* element method

A spectral/*hp* element method, implemented in the open-source code Nektar++[19], is utilized to solve equations (2) and (3). In this method, the computational domain is initially partitioned into macro elements, as illustrated in Figure 8 (Taking the plate at AoA = 15° as an example). Within each element, the solution is expressed as a tensor product of one-dimensional polynomial bases, specifically the modified Jacobi polynomials. The order of the expansion is denoted by $P$, where $P+1$ represents the number of modes in each spatial dimension.

The first-order velocity correction scheme[21], is employed to transform equations (2) and (3) into the velocity Helmholtz equations and the pressure Poisson equation. These transformed equations are then directly solved using a parallel Cholesky decomposition algorithm[22]. On the upstream, upper, and lower boundaries of the computational domain, a Dirichlet-type boundary condition is imposed. A high-order outflow boundary condition is utilized on the downstream boundary. On the body surface, a Dirichlet boundary condition is applied to the velocity components, whereas a high-order Neumann condition is adopted for the pressure[23]. To enhance numerical stability, a DG-mimick spectral vanishing viscosity with a coefficient of 0.1 is incorporated, as outlined in Moural et al.[24].

The governing equation (1) for the body's motion is tackled using a fully implicit Newmark-beta method, as introduced in Ref. [25]. A weak coupling method, as described in Ref. [26], is employed to solve the fluid-structure interaction system holistically.

## B Convergence study

The computational domain is selected as $-40 \leqslant x/c \leqslant 60$, $-40 \leqslant y/c \leqslant 40$ which is proved sufficient in previous studies[14, 15, 18]. The macro elements in the computational domain, as well as near the plate surface, are shown in Fig. 8. To fully resolve the finest flow structures in the boundary layer, the height of elements attached to the wall is $0.003c$. Note that in the spectral/*hp* element method, grid refinement can be achieved by increasing the number of macro elements $N$ or the polynomial order $P$.

A convergence study on the spatial and temporal resolutions is conducted at $\mathrm{AoA} = 15^\circ$, $U^* = 1.54$ ($f_n = 0.65$), $Re = 800$, $M^* = 1$. For the mesh shown in Fig. 8, there are 7634 quadrilaterals and 918 triangles in total (the element number $N = 8552$). Reducing the dimensionless time step $\Delta t^* = \Delta t U_\infty c^{-1}$ from $1/2000$ to $1/4000$ results in a relative difference of 0.1% on the maximum lift coefficient. In addition, there is almost no difference between the $C_L$ of $P = 4$ and $C_L$ of $P = 5$. Table 1 shows the time-averaged drag ($C_D$) and lift ($C_L$) coefficients, the peak-to-peak amplitude ($A_y^*$), and the dominant frequency ($f_y^*$) of the vertical displacement. The mesh with an element number of $N = 3737$ and $P = 4$ already has sufficient accuracy on the force and FIV of the plate. However, to better capture the vortex wake, the mesh with 8552 elements, $P = 4$, and $\Delta t^* = 5\times10^{-4}$ are used in all sim-



CSTR: 32290.14.JUSTC-2025-0023
DOI: 10.52396/JUSTC-2025-0023
*JUSTC*, **2026**, 55(X):

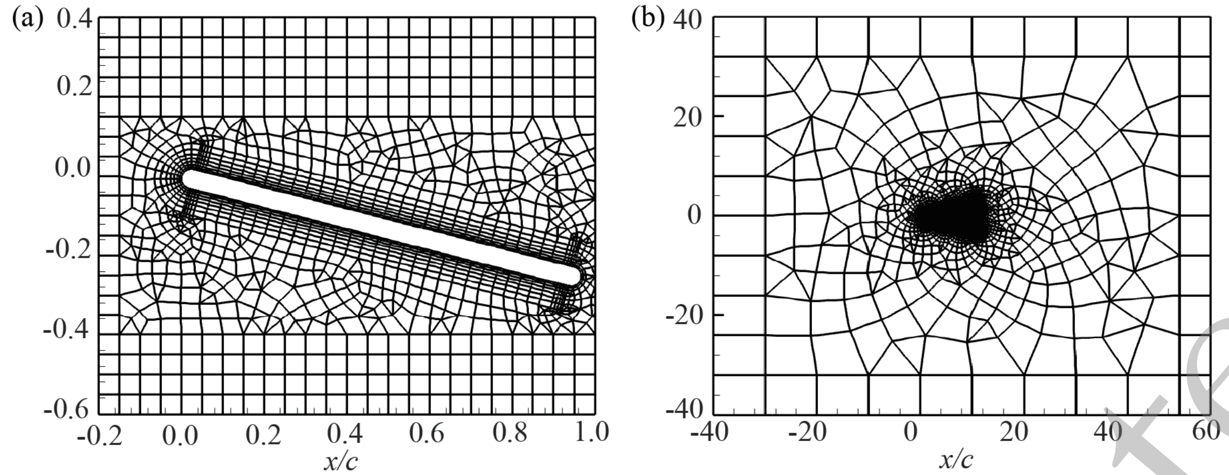


**Fig. 8.** Macro elements in the computational domain for the plate at AoA = 15°. (a) Global view. (b) Near the plate.

**Table 1.** Time-averaged drag and lift coefficients, oscillation amplitude, and dominant frequency for the tested case with $\alpha = 15°$, $U^* = 1.54$, $Re = 800$ and $M^* = 1$.

| N | $P$ | $\Delta t^*$ | $C_D$ | $C_L$ | $A_y^*$ | $f_y^*$ |
|---|---|---|---|---|---|---|
| 3737 | 4 | $5\times10^{-4}$ | 0.3862 | 1.1163 | 0.07420 | 0.4898 |
| 8552 | 4 | $5\times10^{-4}$ | 0.3866 | 1.1180 | 0.07411 | 0.4899 |
| 8552 | 4 | $1\times10^{-3}$ | 0.3875 | 1.1214 | 0.07382 | 0.4902 |
| 8552 | 5 | $2.5\times10^{-4}$ | 0.3863 | 1.1172 | 0.07424 | 0.4898 |

ulations.

## C Validation of the flow-induced vibrations of the cylinder

The flow-induced vibration of a 2-D circular cylinder with bilateral constraint and one vertical degree of freedom is carried out. The diameter-based Reynolds number is $Re = U_\infty D/\nu = 150$ and the mass ratio is $M^* = M/(\rho D^2) = 2$. The reduced velocity varies in the range of $U^* = 3.0-8.0$. The computational domain is $-40D \leqslant x \leqslant 80D$, $-40D \leqslant y \leqslant 40D$ with a total number of 5080 elements and a polynomial order of $P = 5$. The total simulation time is $400DU_\infty^{-1}$ and the time step is $1/2000DU_\infty^{-1}$.

Figure 9 shows that the present results agree well with previous results[27–29]. Here, Ahn et al.[27] implemented a geometrically conservative finite-volume arbitrary Lagrangian-Eulerian (ALE) scheme combined with hybrid mesh techniques to achieve strong-coupled fluid-structure interaction simulations. Borazjani et al.[28] employed a sharp-interface immersed boundary method, adopting a second-order quadratic upstream interpolation (QUICK) scheme for the advection term discretization and a three-point central differencing scheme for viscous and pressure terms. Bao et al.[29] used an ALE method with an explicit time integration scheme for the structural equations.

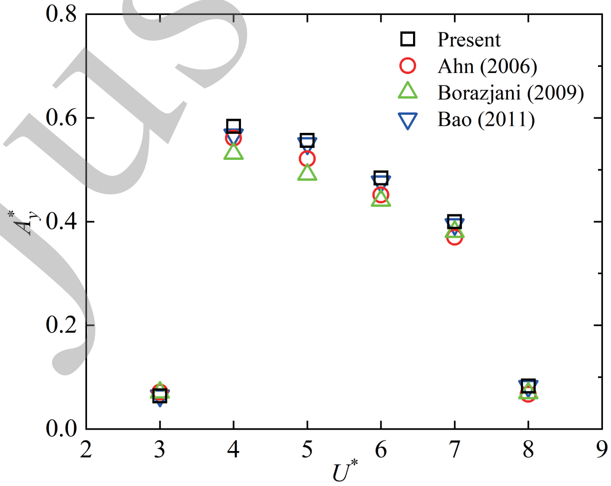


**Fig. 9.** Dimensionless peak-to-peak amplitude of the vertical displacement of the circular cylinder at $Re = 150$. Squares: present simulations; circles: simulation results of Ahn et al.[27]; triangles: simulation results of Borazjani et al.[28]; inverse triangles: simulation results of Bao et al.[29].


CSTR: 32290.14.JUSTC-2025-0023
DOI: 10.52396/JUSTC-2025-0023
JUSTC, 2026, 55(X):

### D The natural frequency of unilateral-constraint system in vacuum

The natural frequency of the unilateral-constraint system in the vacuum is derived in this section. Assuming the maximum jumping height of the body is $a$, indicating the maximum vertical position of the body is $a$, the contacting time between the body and the spring is known from harmonic motion as

$$T_{\text{contact}} = 2\sqrt{\frac{M}{k}}\left(\pi - \arctan\left(\sqrt{\frac{2ak}{Mg}}\right)\right) \tag{D1}$$

During the free motion phase, the body moves at an initial speed of $v_0$, rises to its highest point under the action of gravity, and then falls back. The total time of the free-motion stage is

$$T_{\text{free}} = \frac{2v_0}{g} \tag{D2}$$

Due to the conservation of the mechanical energy, there is

$$v_0 = \sqrt{2ag}. \tag{D3}$$

Therefore,

$$T_{\text{free}} = 2\sqrt{\frac{2a}{g}} \tag{D4}$$

The total period is the sum $T_{\text{free}}$ and $T_{\text{contact}}$

$$T_{\text{total}} = 2\sqrt{\frac{M}{k}}\left(\pi - \arctan\left(\sqrt{\frac{2ak}{Mg}}\right)\right) + 2\sqrt{\frac{2a}{g}} \tag{D5}$$

$$f_{n,\text{unilateral}} = \frac{1}{T_{\text{total}}} \tag{D6}$$

If the body does not leave the sea floor, substituting $a = 0$ into equation (D6) recovers equation (5).





CSTR: 32290.14.JUSTC-2025-0023
DOI: 10.52396/JUSTC-2025-0023
*JUSTC*, **2026**, 55(X):